Understanding InP Nanowire Array Solar Cell Performance by Nanoprobe-Enabled Single Nanowire Measurements

Otnes, Gaute; Barrigón, Enrique; Sundvall, Christian; Svensson, K. Erik; Heurlin, Magnus; Siefer, Gerald; Samuelson, Lars; Åberg, Ingvar; Borgström, Magnus T.

Published in:
Nano Letters

DOI:
10.1021/acs.nanolett.8b00494

2018

Document Version:
Publisher's PDF, also known as Version of record

NANO LETTERS

Letter

Cite This: Nano Lett. 2018, 18, 3038−3046

pubs.acs.org/NanoLett

Understanding InP Nanowire Array Solar Cell Performance by Nanoprobe-Enabled Single Nanowire Measurements

Gaute Otnes,[†] Enrique Barrigón,[†] Christian Sundvall,[‡] K. Erik Svensson,[‡] Magnus Heurlin,[†,‡] Gerald Siefer,[§] Lars Samuelson,[†] Ingvar Åberg,[‡] and Magnus T. Borgström*[,†]

[†]Solid State Physics and NanoLund, Lund University, P.O. Box 118, SE-221 00 Lund, Sweden

[‡]SolVoltaics AB, Scheelevägen 22, SE-223 63 Lund, Sweden

[§]Fraunhofer ISE, Heidenhofstrasse 2, D-79110 Freiburg, Germany

Supporting Information

ABSTRACT: III−V solar cells in the nanowire geometry might hold significant synthesis-cost and device-design advantages as compared to thin films and have shown impressive performance improvements in recent years. To continue this development there is a need for characterization techniques giving quick and reliable feedback for growth development. Further, characterization techniques which can improve understanding of the link between nanowire growth conditions, subsequent processing, and solar cell performance are desired. Here, we present the use of a nanoprobe system inside a scanning electron microscope to efficiently contact single nanowires and characterize them in terms of key parameters for solar cell performance. Specifically, we study single as-grown InP nanowires and use electron beam induced current characterization to understand the charge carrier collection properties, and dark current−voltage characteristics to understand the diode recombination characteristics. By correlating the single nanowire measurements to performance of fully processed nanowire array solar cells, we identify how the performance limiting parameters are related to growth and/or processing conditions. We use this understanding to achieve a more than 7-fold improvement in efficiency of our InP nanowire solar cells, grown from a different seed particle pattern than previously reported from our group. The best cell shows a certified efficiency of 15.0%; the highest reported value for a bottom-up synthesized InP nanowire solar cell. We believe the presented approach have significant potential to speed-up the development of nanowire solar cells, as well as other nanowire-based electronic/optoelectronic devices.

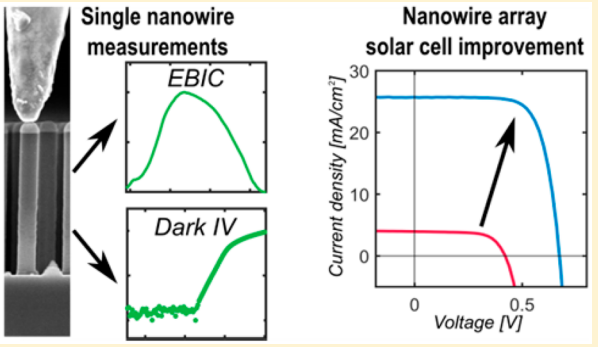

KEYWORDS: *Nanowire, solar cell, nanoprobe, EBIC, power conversion efficiency, InP*

Over the past decade, exciting progress has been made in the field of III−V nanowire solar cell research.[1−7] Advances in large area patterning techniques, most importantly nanoimprint lithography (NIL),[8−10] have opened up for growth of uniform nanowire arrays covering large areas. By exploiting geometry-dependent absorption resonances as predicted by theory,[11,12] strong optical absorption has been demonstrated in such arrays, where the nanowires cover only ∼10% of the surface.[4,6,13,14] The reduced material consumption potentially gives commercially important cost-savings, especially if combined with the possibility of growth on foreign low-cost substrates,[5,15] substrate reuse,[16] or substrate-free synthesis techniques.[17,18] At the same time, relaxed lattice matching requirements in the nanowire geometry[19−22] offers an increased freedom in material combinations to obtain optimized tandem architectures.[23,24]

Improvements in III−V nanowire solar cell performance have been impressive with the current power conversion efficiency (PCE) records at 13.8% and 15.3% for bottom-up synthesized InP[4] and GaAs[6] devices, respectively, and 17.8% for a top-down synthesized InP device.[7] However, to further increase efficiency and make the nanowire solar cell technology competitive with their planar counterparts, a deepened understanding is needed of the link between parameters used for synthesis, material properties, and solar cell performance in these structures. Importantly, nanowire growth is carried out in the kinetically limited growth regime, making it highly sensitive to deviations in growth temperature, substrate preparation,[9,10] and substrate size. This is especially true for the ternary materials needed to obtain the optimal bandgaps for tandem configurations,[23,24] where the nanowire geometry might hold its foremost advantages.[1] Further, processing nanowire solar cell arrays into working devices has proven possible but is relatively labor-intensive and slow in a nonautomated research environment. Therefore, to increase speed of optimization, rapid and reliable characterization of parameters relevant to

Received: February 4, 2018
Revised: April 12, 2018
Published: April 27, 2018

DOI: 10.1021/acs.nanolett.8b00494
Nano Lett. 2018, 18, 3038−3046

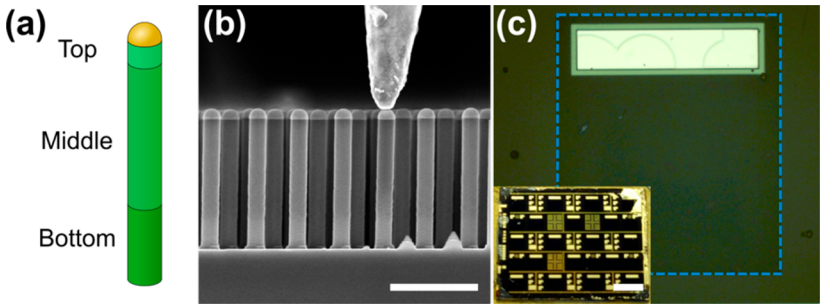

Figure 1. Sample illustrations. (a) Sketch of the nanowire structure, containing a bottom, middle and top segment. The doping of the top segment is n-type (grown with $\chi_{TESn} = 4.3 \times 10^{-5}$) and the bottom segment is *p*-type (χ_{DEZn} varied between runs) for all samples in this paper. As explained in the main text, the middle segment is nominally intrinsic (χ_{PH3} varied between runs) or lightly p-doped (χ_{DEZn} varied between runs). (b) Example cross section SEM image of a nanowire array with the tungsten nanoprobe contacting a single nanowire. The scale bar is 1 μm. (c) Optical microscope image of a 1 × 1 mm^2 processed solar cell, highlighted with the blue dashed line. Inset: Photo of a sample containing a number of cells of different sizes. Scale bar in the inset is 2 mm.

solar cell performance is desired to provide feedback to growth development. Additionally, there is a need for characterization techniques that can be used to separate effects on performance inherent to the as-grown nanowires from effects introduced by the subsequent processing.

In this work, we compare single as-grown nanowire measurements, enabled by a nanoprobe system inside a scanning electron microscope (SEM) with measurements of fully processed nanowire array solar cells (hereafter referred to as "processed solar cells"). The nanoprobe top-contact to the as-grown nanowires on the substrate (Figure 1b) allows us to obtain single nanowire current−voltage ($I-V$) data combined with electron beam induced current (EBIC) measurements. Thus, we can quickly screen key properties for solar cell performance without full vertical processing and provide insight in the relationship between growth conditions and material properties. Correlating with processed solar cells deepens our understanding of the interplay between growth parameters, processing conditions and the solar cell PCE. We note that several highly interesting single nanowire measurements with relevance to solar cells have been performed[25−28] but typically include time-consuming and challenging contacting with help of electron beam lithography. In contrast, nanoprobe systems inside an SEM allow for relatively fast contacting and have previously been used to contact single nanowires to study transport characteristics,[29,30] diffusion lengths,[31,32] doping levels,[33] and Esaki diode characteristics.[34] Here, we demonstrate its usefulness on a number of levels in the development of a nanowire solar cell, through a systematic study of the key parameters determining PCE and correlation with processed solar cells from the same growth runs.

We use this approach to characterize InP nanowire solar cells. After the previous report from our group on an InP nanowire solar cell with a PCE of 13.8%,[4] we adopted a new hexagonal nanowire seed particle pattern, optimized for light absorption[12] and homogeneous ternary nanowire growth.[35] Unfortunately, this denser pattern introduced significant challenges retaining pattern fidelity due to seed particle displacement for which a pre-anneal nucleation step was developed.[10] In addition, growth parameters had to be reoptimized for this pattern with respect to nanowire solar cell performance. Here we demonstrate the usefulness of nanoprobe-enabled single nanowire measurements in the development of nanowire solar cells. Specifically, we use EBIC data to optimize the charge carrier collection properties of single nanowires and thereby improve solar cell short-circuit current density (J_{SC}). Thereafter, we use dark $I-V$ data, both from single nanowires and processed solar cells, to improve recombination characteristics of our device, thereby improving open-circuit voltage (V_{OC}) and fill-factor (FF). Although single nanowire dark $I-V$ data by use of a nanoprobe can also be obtained, for example, inside an atomic force microscope,[36] we emphasize that a key benefit of using the nanoprobe inside an SEM is the ability to simultaneously monitor both charge carrier collection and recombination characteristics of the single nanowires (via EBIC and dark $I-V$, respectively), to ensure optimization taking all aspects of device performance into account. The optimization based on feedback from single nanowire measurements result in InP nanowire solar cell PCE improving from below 2% (noncertified measurement) to 15.0% (certified measurement).

The InP nanowires were grown with three segments for all samples studied here (Figure 1a) with the bottom segment being p-type, the middle segment being nominally intrinsic or lowly p-doped, and the top segment being n-type. Note the use of a long middle segment between the p- and the n-type segments, intended to create a long depletion region where the built-in field enhances carrier collection. The length of each segment was monitored in situ by use of optical reflectance spectroscopy,[37] and the desired lengths were achieved by adjusting the growth time. After growth, the samples were cleaved, glued to a 90° SEM stub by silver paste, and loaded into a Hitachi SU8010 SEM. A nanoprobe system from Kleindiek Nanotechnik with piezoelectronic positioning control was used to form contact between a tungsten nanoprobe and the gold nanoparticle on top of single nanowires (Figure 1b). In this configuration EBIC and dark $I-V$ characteristics of 4−5 single nanowires on each sample were obtained. Screening a sample in this way takes around 1.5 h, including sample mounting and loading. Additionally, some samples were processed into 1 × 1 mm^2 solar cells (Figure 1c) and measured in a commercial solar simulator Oriel Sol1A under AM1.5g-similar solar illumination at 1-sun intensity. Further details on the synthesis and measurement procedures can be found in Methods.

Solar cell PCE is typically calculated from the maximum power point, P_{mpp}, extracted from the light $I-V$ curve. However, it can also be represented as the product of the three parameters J_{SC}, V_{OC}, and FF, which are partly interdependent and must all be optimized with respect to

DOI: 10.1021/acs.nanolett.8b00494
Nano Lett. 2018, 18, 3038−3046

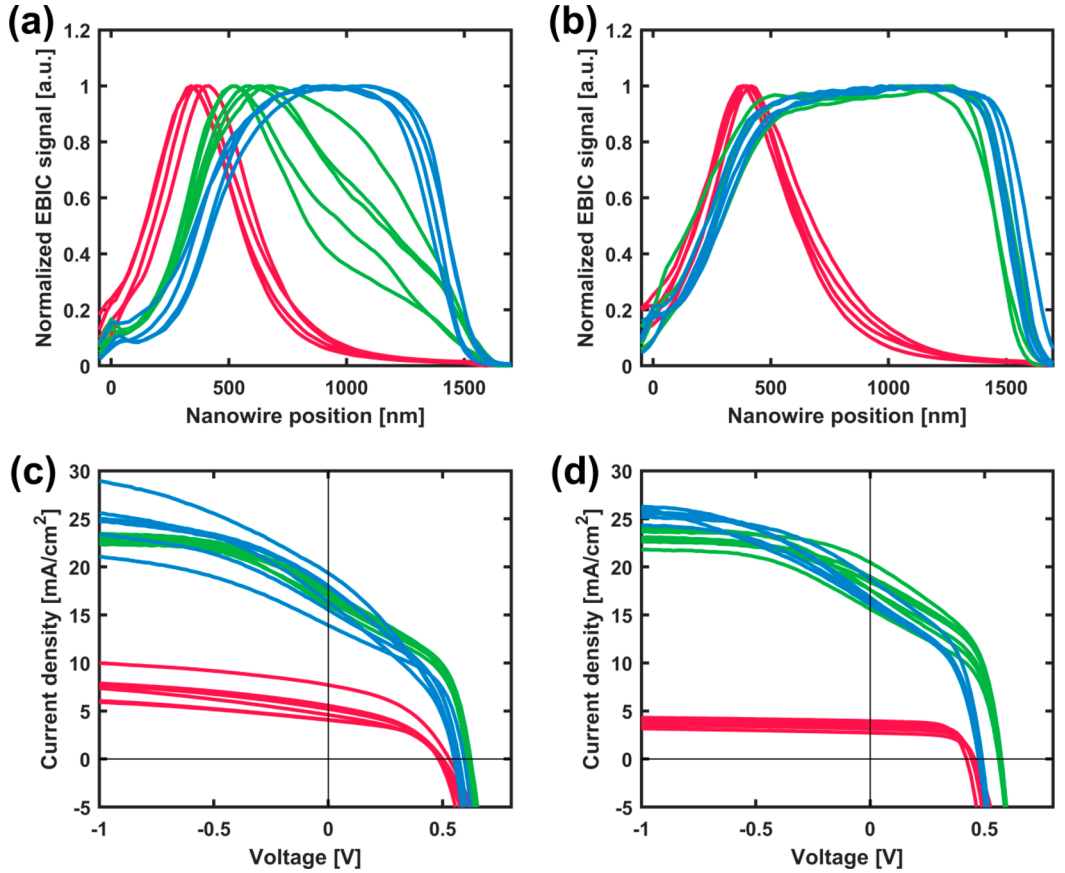

Figure 2. Optimizing electron beam induced current (EBIC) profiles by tuning growth parameters, resulting in improved J_{SC}. EBIC profiles for single nanowires/light $I-V$ curves for processed solar cells, grown with different (a)/(c) PH_3 flow through the entire nanowire; $\chi_{PH3} = 0.69 \times 10^{-2}$ (red), $\chi_{PH3} = 1.39 \times 10^{-2}$ (green), and $\chi_{PH3} = 1.92 \times 10^{-2}$ (blue), and (b)/(d) DEZn flow in the middle segment; $\chi_{DEZn} = 0$ (red), $\chi_{DEZn} = 0.5 \times 10^{-7}$ (green), and $\chi_{DEZn} = 2.1 \times 10^{-7}$ (blue). For the EBIC profiles, the nanowire position equals zero indicate the nanowire−substrate interface.

performance. We will start by discussing J_{SC}, which is dependent on both the absorption and carrier collection efficiency. Strong absorption in our dense arrays with optimized nanowire diameter have been confirmed by both modeling and experiments,[12,13] allowing us to focus here on understanding and optimizing the carrier collection efficiency. We use a series of samples with bottom-, mid-, and top-segment lengths of 400 ± 30, 1000 ± 70, and 80 ± 15 nm, respectively, as measured by optical reflectance[37] with the errors indicating the variation between samples. This gives a total nanowire length of 1500 ± 70 nm, and the small variation in segment and total length ensures that the carrier generation profile in each segment and in total can be considered similar in all samples. While the bottom and top segment are p- and n-doped, respectively, the middle segment is nominally intrinsic (Figure 1a) in an attempt to have a long absorber region where an electric field enhances carrier collection. All samples were grown with three substrates in the growth run, allowing for both single nanowire and processed solar cell measurements.

As a starting point, we characterized a sample where the bottom segment is lowly p-doped ($\chi_{DEZn} = 0.59 \times 10^{-5}$), whereas the middle segment is nominally intrinsic. EBIC profiles of all measured nanowires on this sample are plotted with red in Figure 2a. We observe the peak of the EBIC profile, indicating the junction position, at the p−i interface. Because the optical generation rate is strongest close to the top of the nanowire,[38] such a deep junction will lead to poor carrier collection. This is confirmed by $I-V$ curves from the processed solar cells under 1 sun illumination (Figure 2c, red line), where J_{SC} falls in the range of only 4−8 mA/cm^2 and the PCE is below 2%. A junction position at the p−i interface shows that the nominally intrinsic InP nanowire segments are in fact n-type, in accordance with literature on nominally intrinsic bulk InP.[39] Depending on growth conditions for bulk InP, the n-type background doping has been related to P_{In}-antisites (P-rich growth conditions)[40,41] and P-vacancies (P-poor growth conditions).[39,42] In an attempt to determine which native defect is dominating in our case, and to compensate it, we varied the PH_3 flow between runs. Upon decreasing the PH_3 flow to $\chi_{PH3} = 0.35 \times 10^{-2}$ from the reference level ($\chi_{PH3} = 0.69 \times 10^{-2}$) we observe that the shape of the EBIC profile is largely unchanged (not shown in the figure), while increasing the PH_3 flow to $\chi_{PH3} = 1.39 \times 10^{-2}$ (Figure 2a, green line) and $\chi_{PH3} = 1.92 \times 10^{-2}$ (Figure 2a, blue line) leads to a significant change in the EBIC profile shape. From a Gaussian-like profile shape indicating a fairly abrupt junction for low PH_3 flows, an evolution toward a flatter profile is seen for increasing PH_3 flows. This indicates that nonintentional doping via P-vacancies is reduced using higher PH_3 flows, which we speculate results in the development of a longer, more well-defined depletion region between the intentionally grown n- and p-type segments which enhances carrier collection throughout this region.

As a second strategy to improve the EBIC profile, we introduced DEZn during growth of the middle segment to compensate for the n-type background doping (Figure 2b) for samples grown with $\chi_{PH3} = 0.69 \times 10^{-2}$ (reference level in PH_3-

DOI: 10.1021/acs.nanolett.8b00494
Nano Lett. 2018, 18, 3038−3046

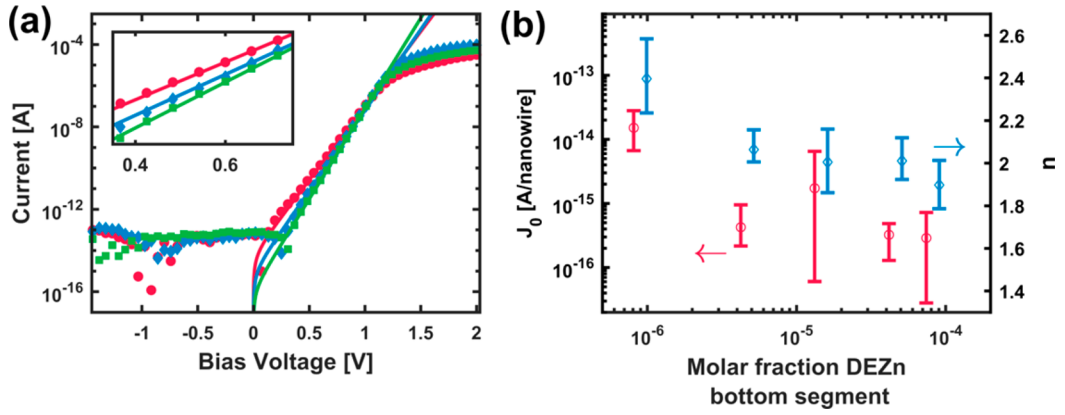

Figure 3. Using single nanowire dark $I-V$ data to extract key diode quality parameters. (a) Example single nanowire dark $I-V$ curves from three different samples grown with different DEZn molar fraction in the bottom segment: $\chi_{DEZn} = 0.09 \times 10^{-5}$ (red circles), $\chi_{DEZn} = 0.47 \times 10^{-5}$ (blue diamonds), $\chi_{DEZn} = 4.63 \times 10^{-5}$ (green squares). Solid lines show fits to the diode equation (eq 3) while the inset shows a zoom-in of the fitted data range. Note that the current density level between −1.5 and 0.2 V is below the noise floor in the measurement. (b) Extracted dark saturation current densities (red circles, left y-axis) and ideality factors (blue diamonds, right y-axis) from curves such as the ones presented in (a). The data points are averages of the measured nanowires on each sample with the error bars indicating the maximum and minimum values measured.

variation experiment). We see that even the lowest molar fraction of DEZn tested, $\chi_{DEZn} = 0.5 \times 10^{-7}$ (green line), gives a significant improvement of the EBIC profile, while a further increase to $\chi_{DEZn} = 1.0 \times 10^{-7}$ (not shown) and $\chi_{DEZn} = 2.1 \times 10^{-7}$ (blue line) gives no significant further improvement. Again, we attribute the flat EBIC profile to a lowering of the effective doping in the middle segment toward more intrinsic levels, making depletion of this segment possible, and hence introducing a drift field which improves carrier collection efficiency.

Looking at the one-sun $I-V$ curves (Figure 2c,d) of processed solar cells for the samples grown with different PH_3 flows and different DEZn flows in the middle segment, we see that the improved carrier collection as indicated by the EBIC profiles correlates with a significant improvement of J_{SC} for both series. Note that the improvement in J_{SC} is significant despite the occurrence of a kink in the $I-V$ curve between approximately −0.5 and 0.5 V, which reduces the device performance. This "s-shaped" $I-V$ curve behavior will be discussed further later in this paper. For now we consider the current density at −1 V as the potentially achievable short circuit current density, $J_{SC,pot}$, for these nanowires, and observe that the adjustments to the growth procedure has improved $J_{SC,pot}$ from ∼5−10 to ∼25 mA/cm^2.

As a next step, we aim for improving the V_{OC} and FF in our devices. Theoretically, the V_{OC} is given by

$$V_{OC} \approx \frac{nkT}{e} \times \ln\left(\frac{J_{SC}}{J_0}\right) \quad (1)$$

where n is the ideality factor of the diode, k is the Boltzmann constant, T is the temperature, e is the elementary charge, and J_0 is the dark saturation current density. The key parameter determining the V_{OC} is J_0, which can vary by orders of magnitude depending on the recombination characteristics of the device. A general expression for the FF cannot be derived from basic theory, but as a benchmark in our discussion we will assume an empirical expression found for Si solar cells[43]

$$FF = \frac{v_{OC} - \ln(v_{OC} + 0.72)}{v_{OC} + 1} \quad (2)$$

where v_{OC} is a normalized open circuit voltage, $v_{OC} = V_{OC}/(nkT/e)$. For a given V_{OC}, we find from eq 2 that the achievable FF is reduced for increasing values of n. Parasitic resistances typically reduce the FF compared to the maximum achievable value given in eq 2.[43]

From eqs 1 and 2, we identify that J_0 and n are key parameters to improve V_{OC} and FF in our devices. These parameters are typically extracted by fitting the exponential region of the solar cell $I-V$ measured in the dark to the diode equation

$$J = J_0 \times (e^{-eV/nkT} - 1) \quad (3)$$

Again, the nanoprobe proves useful because it can be used to quickly obtain $I-V$ characteristics from the single nanowires, allowing assessment of the as-grown diode quality and recombination characteristics. As an example, dark $I-V$ characteristics of nanowires from three different samples are plotted in Figure 3a, together with fits to the diode equation (eq 3). The three samples were grown with different DEZn flow in the bottom segment, to illustrate how changes in diode quality can be efficiently screened for varying growth conditions. In Figure 3b, the extracted average J_0 and n values for these three samples are plotted together with samples using an additional two DEZn flows. Changing the DEZn flow in the p-segment from $\chi_{DEZn} = 0.09 \times 10^{-5}$ to $\chi_{DEZn} = 0.47 \times 10^{-5}$ lowers J_0 by almost 2 orders of magnitude and gives a substantial improvement in n. However, increasing the DEZn flow used in the bottom segment further does not give any major additional improvement.

Note that for the DEZn flows lower than $\chi_{DEZn} = 4.6 \times 10^{-5}$ during growth of the bottom segment, the shape of the EBIC profile remains largely unchanged as a Gaussian-like peak, while the peak position is pushed somewhat higher in the nanowire (see Supporting Information). However, for $\chi_{DEZn} > 4.6 \times 10^{-5}$ we observe an improvement of the EBIC profile similar to intentionally introducing a low flow of DEZn in the middle segment (Figure 2b). We ascribe this to a carry-over effect of Zn, where an overpressure of Zn lingers after the DEZn flow is switched off, from excess Zn stored in the gold seed particle and elsewhere in the reactor interior.[32,44]

DOI: 10.1021/acs.nanolett.8b00494
Nano Lett. 2018, 18, 3038−3046

An interesting question at this point is how well the as-grown single nanowire dark $I-V$ characteristics translate to a processed solar cell. In Figure 4a, we plot an example of dark $I-V$ curves for processed solar cells (blue filled circles) and for single nanowires (red open squares) from the same growth run, where the single nanowire current densities have been scaled by the areal nanowire density of 4.65×10^8 nanowires/cm^2. The exponential regions of the processed solar cells and the single nanowires are remarkably similar, strongly indicating that the solar cell dark $I-V$ characteristics in these devices are dominated by the as-grown nanowire performance in this region. This confirms the excellent uniformity of the single nanowires in our arrays. At forward bias, however, the subexponential behavior due to series resistance is seen at higher currents in the single nanowires than in the processed solar cells, which we ascribe to a superior contact quality of the probe−gold−nanowire as compared to the ITO−nanowire contact. To illustrate how the processed solar cell vs single nanowire comparison might vary between different samples, we return to the three samples grown with different DEZn flow in the middle segment (Figure 2b,d). In Figure 4b, we plot the extracted dark $I-V$ parameters for both single nanowires and processed solar cells. We find an overlap of the ranges of extracted J_0 values for the single nanowires and the processed solar cells (indicated by error bars in Figure 4b) with deviation between average-values less than a factor of 3. For the extracted n values, a similar overlap is present for two of the samples, where the average-values deviate less than 6%. However, for the sample with no DEZn during growth of the middle segment, there is no overlap in the range of extracted values, and a deviation from 2.2 to about 3.5 in the average n measured for the as-grown single nanowires and processed solar cells, respectively. We have observed this also for some other samples, where the processed solar cell n is typically higher than 3 (much higher than for the single nanowire). We ascribe this to device characteristics dominated by a poor nanowire−ITO contact.

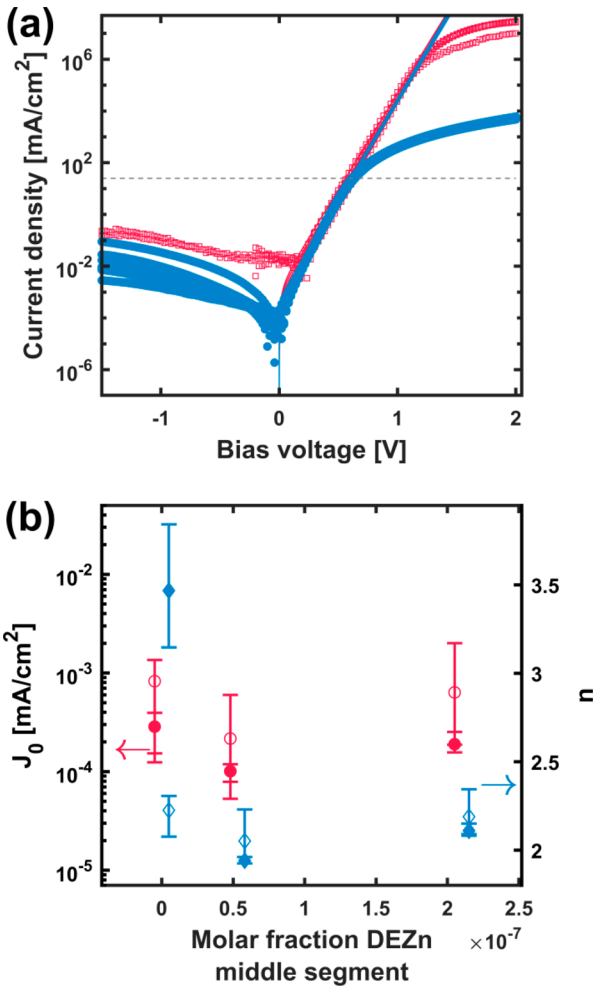

Figure 4. Comparing dark $I-V$ characteristics of single nanowires and processed solar cells. (a) An example of dark $I-V$ curves for processed solar cells (blue filled circles) and single nanowires (red open squares) plotted together, where the single nanowire characteristics have been scaled by the areal density of the nanowire array. Solid lines show fits to the diode equation (eq 3) in the exponential regions. The dashed gray line indicates a good J_{SC} value at a current level of 25 mA/cm^2. Note that the current density level between −1.5 and 0.2 V is below the noise floor in the single nanowire measurement. (b) Comparison of the extracted J_0 (red circles, left y-axis) and n (blue diamonds, right y-axis) values for single nanowires (open symbols) and processed solar cells (filled symbols) for three samples grown with different DEZn flow in the middle segment. The data points are averages of the measured nanowires/cells on each sample, with the error bars indicating the maximum and minimum values measured. EBIC and light $I-V$ characteristics for these three samples are shown in Figure 2b,d, respectively.

Looking at the extracted single nanowire parameters in Figure 4b, a striking feature is the small variation in the dark $I-V$ parameters between the different samples. Comparing Figure 4b with Figure 2b, this small variation in J_0 and n between samples is strongly contrasting the large shift in the EBIC profiles when using higher DEZn flow in the middle segment. We have observed relatively constant dark $I-V$ characteristics also when varying other growth parameters, such as the PH_3 flow (in the range of flows shown in Figure 2a), the growth temperature (in the range 430−450 °C) and the DEZn flow in the bottom segment (for $\chi_{DEZn} > 0.47 \times 10^{-5}$, see Figure 3b). The values for J_0 and n for all tested variations are limited downward to $\sim 2 \times 10^{-5}$ mA/cm^2 and ∼1.9, respectively. We conclude that while varying the growth parameters can have a strong influence on the carrier collection properties of the device, any influence on the diode recombination characteristics in our devices is masked by another dominating factor.

A likely factor affecting diode recombination characteristics is the nanowire surface. Several studies, both theoretical[45−47] and experimental,[3,6,27] have shown that the surface can have a detrimental impact on nanowire solar cell performance. We would like to point out that using the term surface recombination as commonly used for planar solar cells, that is, recombination at the front surface, is not suitable for our devices. Rather, in the axial junction configuration[1] used here we are concerned with a large surface area (the nanowire sidewalls) intersecting the active regions of the device. Recombination at such a surface is in bulk devices referred to as perimeter recombination, and the resulting recombination current density have a dependence on the perimeter to cell area ratio (p/A).[48,49] In our devices, we have an extremely high p/A of about 200 000 cm^{-1}. As a comparison, perimeter recombination have been reported to dominate planar $Ga_{0.5}In_{0.5}P$ solar cell recombination characteristics for $p/A \geq 40$ cm^{-1}.[50] We consistently find n-values close to 2 (Figure 3 and 4), in agreement with typical perimeter recombination in the depletion region.[51−53]

DOI: 10.1021/acs.nanolett.8b00494
Nano Lett. 2018, 18, 3038−3046

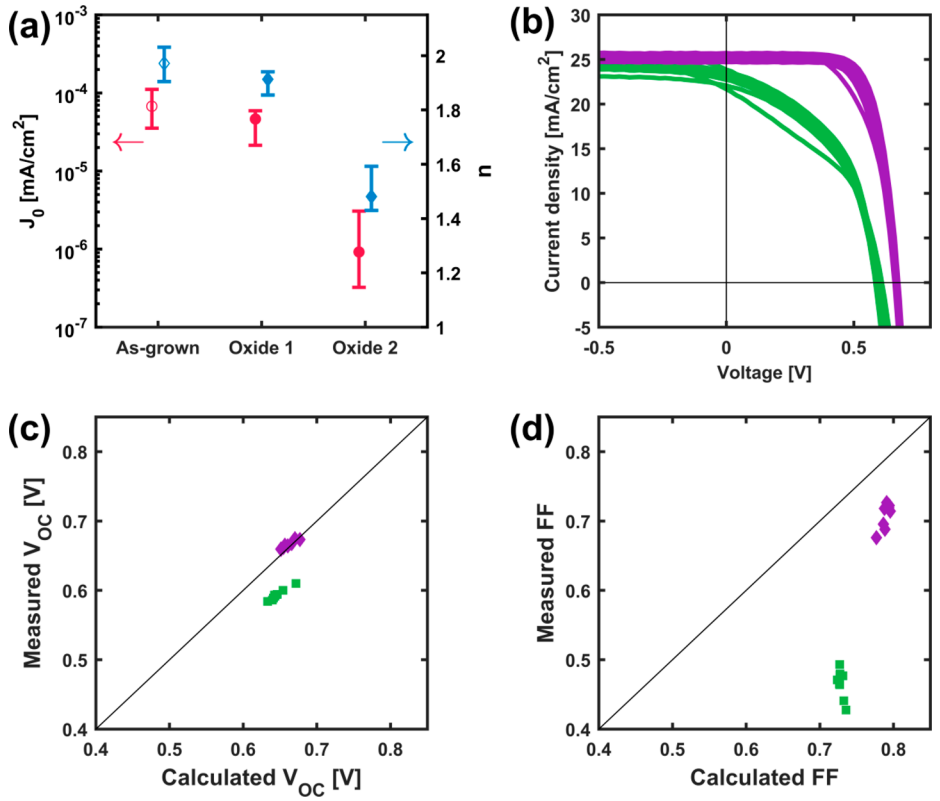

Figure 5. Effect of different SiO_x deposition procedures on dark and light $I-V$ characteristics. (a) Extracted J_0 (red circles, left axis) and n (blue diamonds, right axis) for as-grown single nanowires (open symbols) and processed solar cells (filled symbols) using Oxide 1 and 2. The data points are averages of the measured nanowires/cells on each sample, with the error bars indicating the maximum and minimum values measured. (b) Light $I-V$ for fully processed solar cells using Oxide 1 (green) and Oxide 2 (purple). The difference between Oxide 1 and 2 deposition procedure is explained in the main text. (c) Measured V_{OC} values compared to values calculated from J_0 and n values by eq 1 for cells processed using Oxide 1 (green) and Oxide 2 (purple). (d) Same as in (c) but for FF values, calculated by eq 2.

No suitable high bandgap lattice matched III−V material exists to provide epitaxial passivation of InP, such as InGaP[3,27] and AlGaAs[6] used to passivate GaAs nanowires. However, a recent study by Black et al.[54] has shown how an oxide deposited on the surface by atomic layer deposition (ALD) can significantly enhance the photoluminescence lifetime and internal quantum yield of InP nanowires. With this in mind, we look to the processing scheme we use to fabricate our nanowire solar cells, where the first step is the deposition of a SiO_x layer to protect and avoid shortening of the junction. To test whether the deposition procedure of this oxide could potentially change the device performance, we compare two different standard oxides deposited in our lab. These oxides will hereafter be referred to as Oxide 1 and 2, and we note that all samples presented earlier in this paper were processed using Oxide 1 (for further detail on the oxides and deposition procedures, see Methods). For the comparison, we deposited the oxides on samples grown in the same growth run, with bottom segment grown with $\chi_{DEZn} = 1.11 \times 10^{-5}$, middle segment grown with $\chi_{DEZn} = 0.5 \times 10^{-7}$, and segment lengths of 700, 1500, and 70 nm for bottom, middle and top, respectively. In Figure 5a, extracted J_0 and n values are plotted for the as-grown single nanowires, and the processed solar cells using Oxide 1 and Oxide 2. While the deposition of Oxide 1 does not alter the dark $I-V$ characteristics significantly from the as-grown nanowires (in agreement with results presented in Figure 4), Oxide 2 lowers the average J_0 from 4.6×10^{-5} to 9×10^{-7} mA/cm^2 and the average n from 1.91 to 1.48.

In Figure 5b, the light $I-V$ characteristics of the solar cells processed with Oxide 1 (green lines) and Oxide 2 (purple lines) is shown. A clear improvement in both V_{OC} and FF is observed when going from Oxide 1 to Oxide 2. To better understand this improvement and how it relates to the improvement in the dark $I-V$ characteristics (Figure 5a), it is instructive to compare the measured V_{OC} and FF values to the ones calculated from eq 1 and 2, using J_0 and n from fits to the processed solar cell dark $I-V$ curves. Figure 5c,d shows plots of the calculated compared to measured V_{OC} and FF values, respectively, where the diagonal lines indicate when the values would be identical. Starting with Oxide 1, the measured V_{OC} values (Figure 5c, green squares) are on average 0.06 V lower than the diagonal line which is what one could expect from eq 1 using the extracted n and J_0 values (Figure 5a). Similarly, the measured FF values (Figure 5d, green squares) for cells with Oxide 1 lie on average 0.25 below the values calculated by eq 2. To understand these discrepancies, we look at the key assumption made in our use of eq 1 and 2: the recombination characteristics of the device are the same under illumination as in the dark. Then we can use the parameters from the dark $I-V$ curve (J_0 and n) to calculate light $I-V$ parameters (V_{OC} and FF). In other words, we have assumed that the superposition principle holds, thus we find the light $I-V$ characteristics by adding J_{SC} to the dark $I-V$ characteristics, $J_L(V) = J_D(V) + J_{SC}$. While this approximation is most often valid, cases of deviation from the superposition principle are known, for example, for planar Si,[55] CIGS[56] and CdTe[57] solar cells. For nanowire solar

DOI: 10.1021/acs.nanolett.8b00494
Nano Lett. 2018, 18, 3038−3046

cells, a recent modeling study from Chen et al. found that a poor nanowire sidewall surface can give a much higher recombination rate under illumination than in the dark, leading to a breakdown of the superposition principle.[58] We speculate that similar effects might play out in our devices processed using Oxide 1 (Figure 2c,d and Figure 5b). Contrasting the cells with Oxide 1, the V_{OC} values for cells with Oxide 2 (purple diamonds) fall well on the diagonal line in Figure 5c, implying a surface improvement sufficient to establish validity of the superposition principle. The FF values for Oxide 2 in Figure 5d being a little lower (on average 0.07) than the calculated maximum achievable value is ascribed to the fairly high series resistance in our devices (Figure 4a), and possibly to the empirical expression derived for Si solar cells (eq 2) not being entirely valid for our InP nanowire solar cells.

Additional to mitigation of excess recombination under illumination, part of the enhanced performance is reflected in the improved dark $I-V$ characteristics (Figure 5a). However, for the V_{OC} both J_0 and n are lowered when going from Oxide 1 to 2. The new values result in only a minor improvement in the calculated V_{OC} values between the cells with Oxide 1 and Oxide 2 (as indicated by the small shift in x-direction in Figure 5c, between green squares and purple diamonds). The lowering of n however, has a significant effect on the calculated FF as shown equivalently in Figure 5d.

The improvement in dark and light $I-V$ characteristics (Figure 5) when using Oxide 2 instead of Oxide 1 indicates a passivation effect of the sidewall surface. Determining the mechanism behind is beyond the scope of our current study, but we note that Oxide 2 uses TMA as one of the precursors (see Methods for deposition conditions), which has been ascribed to give a "self-cleaning" effect of planar III−V semiconductor surfaces.[59−61] Another possible contributing factor is effects of the surface oxide on device performance through charge transfer and field-effects, which can be especially significant in large surface-to-volume ratio structures like nanowires.[62] We believe that there is potential to further optimize the passivating oxide, and hence the nanowire solar cell performance. The nanoprobe measurements will be useful in the development of surface passivation, either by in situ or ex situ methods. Ex situ passivation would likely require some processing to provide access to contact the nanowires by the nanoprobe. We note that, as the perimeter becomes less dominant due to improved passivation, also recombination in other parts of the diode will become influential, and one will likely need more sophisticated analysis of the dark $I-V$ curve than the simple single diode model (eq 3) used here.

The best cell from Figure 5 has further been measured at Fraunhofer ISE CalLab PV Cells. Initially the cell's external quantum efficiency was measured and used for the spectral mismatch correction of the sun simulator. At the sun simulator the cell operated at V_{OC} conditions under illumination for approximately 30 min and afterward was held at P_{mpp} for another 90 min. A relative increase in maximum power of 3.9% was observed within this period. A stabilized $I-V$ curve measurement was then performed which resulted in AM1.5g $I-V$ parameters of J_{SC} = 26.64 mA/cm^2, V_{OC} = 729.9 mV, FF = 77.04%, and a PCE of 15.0% (J_{SC} and PCE refer to designated cell area excluding the busbar). This PCE is the highest reported value for a bottom-up synthesized InP nanowire solar cell, while the J_{SC} is the highest reported value for a bottom-up synthesized nanowire solar cell regardless of material.

Lastly, we note how the nanoprobe inside the SEM will be a powerful tool to reveal and quantify effects of a number of poor performing nanowires which might limit the overall solar cell performance in an inhomogeneous array of nanowires, as discussed by Mikulik et al.[36] However, in our arrays we observe an excellent uniformity between individual nanowires both in terms of length and diameter (Figure 1b), EBIC characteristics (Figure 2a,b), and dark $I-V$ characteristics (Figures 3b and 4). We ascribe the uniformity to the high pattern fidelity in our hexagonal nanowire arrays,[10] ensuring all nanowires to experience similar growth conditions.

In conclusion, we have shown how the use of a nanoprobe to contact single nanowires inside a SEM can be of value to nanowire solar cell development in a number of ways. First, it can efficiently provide direct feedback on carrier collection and recombination properties of the as-grown nanowires to more quickly optimize the material properties and understand its relation to the growth conditions. Second, by correlating these results with performance of fully processed nanowire array solar cells, we can better understand the effects of processing on the nanowire solar cell performance. We have utilized this technique to improve the J_{SC}, V_{OC}, and FF of our devices, resulting in a more than 7-fold improvement in solar cell *PCE*, from less than 2% (Figure 2c,d, red curves, noncertified) to 15.0% (certified by Fraunhofer ISE).

We believe that the use of single nanowire measurements as described here holds great potential in accelerating the development toward high performing nanowire solar cells, also in more complex tandem geometries, as well as other nanowire devices such as photodetectors, light emitting diodes, and lasers.

Methods. *Nanowire Growth.* The InP nanowires studied were grown from arrays of Au seed particles (discs of 0.19 μm diameter, 0.06 μm height, in a hexagonal array of 0.50 μm pitch) placed on full 2 in. InP/Zn (111)B wafers by nanoimprint lithography, as described previously.[10] The wafer was split into smaller pieces of approximately 1 × 1 cm^2 and the desired number of pieces were loaded into a laminar flow metalorganic vapor phase epitaxy (MOVPE) reactor (Aixtron 200/4), using a working pressure of 100 mbar, hydrogen (H_2) as a carrier gas, and a total gas flow of 13 L/min. After a preanneal nucleation step to improve pattern preservation,[10] the sample was annealed at 550 °C under a phosphine (PH_3)/H_2 mixture, and cooled down to the growth temperature of 440 °C. Then, nanowire growth was initiated by adding trimethylindium (TMIn), diethylzinc (DEZn), and hydrogen chloride (HCl) to the gas mixture. The molar fraction of HCl used to suppress radial growth[63] was $\chi_{HCl} = 4.6 \times 10^{-5}$ throughout the nanowire for all samples, whereas the TMIn molar fraction was $\chi_{TMIn} = 5.9 \times 10^{-5}$ for the bottom and top segments, and $\chi_{TMIn} = 7.4 \times 10^{-5}$ for the middle segment. The PH_3 flow was kept constant throughout the nanowire at a flow of $\chi_{PH3} = 0.69 \times 10^{-2}$. The dopant flow in the bottom p-segment was varied from $\chi_{DEZn} = 0.09 \times 10^{-5}$ to 8.24×10^{-5} between different samples. The middle segment was grown nominally intrinsic or lowly p-doped, χ_{DEZn} varied from 0 to 2.1×10^{-7} between different samples. The top n-segment was doped with tetraethyltin (TESn), grown with $\chi_{TESn} = 4.3 \times 10^{-5}$ for all samples.

Single Nanowire Measurements. All measurements shown here were taken at room temperature with currents and voltages measured by a Keithley 2635B sourcemeter, and EBIC taken at a beam accelerating voltage of 5 kV and a beam current

DOI: 10.1021/acs.nanolett.8b00494
Nano Lett. 2018, 18, 3038−3046

in the range of tens of pA (from reference measurements by a Faraday cup). These beam settings ensure full excitation volume[64] within the single nanowire, and give EBIC levels on the order of 1×10^{-10} A, comparable to current levels in a single nanowire in our array under one sun illumination ($\sim 5 \times 10^{-11}$ A).

Solar Cell Processing. The solar cells were processed similarly as in ref 6 with top contact made using indium tin oxide (ITO) with Ti/Au busbars.

Oxide 1 is a SiO_x deposited in a Veeco/CNT Fiji ALD chamber, at 250 °C and using bis(diethylamino)silane (BDEAS) and O_2-plasma chemistry. At a pressure of 1 mTorr, 750 cycles were performed where each cycle consisted of 1.25 s of BDEAS. Carrier gas flow was 40 sccm of Ar and plasma gas flow 60 sccm of O_2. This resulted in a 0.07 μm thick oxide on the nanowires as measured by SEM.

Oxide 2 is deposited in a Veeco/CNT Savannah ALD chamber, at 255 °C and using a trimethylaluminum (TMAl)/tris(tert-butoxy)silanol (TTBS) chemistry, reported to give a SiO_x film with low Al content (<1 at. %).[65] Using N_2 as a carrier gas and a base pressure of approximately 80 mTorr, 18 deposition cycles were performed where each cycle consisted of one 0.06 s pulse of TMAl, followed by three 3 s pulses of TTBS. This resulted in a 0.04 μm thick oxide on the nanowires as measured by SEM.

■ ASSOCIATED CONTENT

Supporting Information

The Supporting Information is available free of charge on the ACS Publications website at DOI: 10.1021/acs.nanolett.8b00494.

Additional EBIC profiles (PDF)

■ AUTHOR INFORMATION

Corresponding Author

*E-mail: magnus.borgstrom@ftf.lth.se.

ORCID

Gaute Otnes: 0000-0002-4241-5234

Magnus T. Borgström: 0000-0001-8061-0746

Author Contributions

The manuscript was written through contributions from all authors. All authors have given approval to the final version of the manuscript.

Notes

The authors declare no competing financial interest.

■ ACKNOWLEDGMENTS

This work was performed within NanoLund and supported by Myfab, the Swedish Research Council (Vetenskapsrådet), the Swedish Foundation for Strategic Research (SSF), the Knut and Alice Wallenberg Foundation and the Swedish Energy Agency. This project has received funding from the *European Union's Horizon 2020 research and innovation programme* under Grant Agreement 641023 (Nano-Tandem) and under the Marie Sklodowska-Curie Grant Agreement 656208. This publication reflects only the author's views and the funding agency is not responsible for any use that may be made of the information it contains. The authors thank Dr. Nicklas Anttu, Yang Chen, and Anders Kvennefors for useful discussions.

■ REFERENCES

(1) Otnes, G.; Borgström, M. T. *Nano Today* **2017**, *12*, 31−45.

(2) Goto, H.; Nosaki, K.; Tomioka, K.; Hara, S.; Hiruma, K.; Motohisa, J.; Fukui, T. *Appl. Phys. Express* **2009**, *2* (3), 035004.

(3) Mariani, G.; Scofield, A. C.; Hung, C.-H.; Huffaker, D. L. *Nat. Commun.* **2013**, *4*, 1497.

(4) Wallentin, J.; Anttu, N.; Asoli, D.; Huffman, M.; Åberg, I.; Magnusson, M. H.; Siefer, G.; Fuss-Kailuweit, P.; Dimroth, F.; Witzigmann, B.; Xu, H. Q.; Samuelson, L.; Deppert, K.; Borgström, M. T. *Science* **2013**, *339*, 1057−1060.

(5) Yao, M.; Cong, S.; Arab, S.; Huang, N.; Povinelli, M. L.; Cronin, S. B.; Dapkus, P. D.; Zhou, C. *Nano Lett.* **2015**, *15* (11), 7217−7224.

(6) Åberg, I.; Vescovi, G.; Asoli, D.; Naseem, U.; Gilboy, J. P.; Sundvall, C.; Dahlgren, A.; Svensson, K. E.; Anttu, N.; Björk, M. T.; Samuelson, L. *IEEE J. Photovoltaics* **2016**, *6* (1), 185−190.

(7) van Dam, D.; van Hoof, N. J. J.; Cui, Y.; van Veldhoven, P. J.; Bakkers, E. P. A. M.; Gómez Rivas, J.; Haverkort, J. E. M. *ACS Nano* **2016**, *10* (12), 11414−11419.

(8) Mårtensson, T.; Carlberg, P.; Borgström, M. T.; Montelius, L.; Seifert, W.; Samuelson, L. *Nano Lett.* **2004**, *4* (4), 699−702.

(9) Pierret, A.; Hocevar, M.; Diedenhofen, S. L.; Algra, R. E.; Vlieg, E.; Timmering, E. C.; Verschuuren, M. A.; Immink, G. W. G.; Verheijen, M. A.; Bakkers, E. P. A. M. *Nanotechnology* **2010**, *21* (6), 065305.

(10) Otnes, G.; Heurlin, M.; Graczyk, M.; Wallentin, J.; Jacobsson, D.; Berg, A.; Maximov, I.; Borgström, M. T. *Nano Res.* **2016**, *9* (10), 2852−2861.

(11) Hu, Y.; LaPierre, R. R.; Li, M.; Chen, K.; He, J.-J. *J. Appl. Phys.* **2012**, *112* (10), 104311.

(12) Anttu, N.; Xu, H. Q. *Opt. Express* **2013**, *21* (May), A558.

(13) Anttu, N.; Abrand, A.; Asoli, D.; Heurlin, M.; Åberg, I.; Samuelson, L.; Borgström, M. T. *Nano Res.* **2014**, *7* (6), 816−823.

(14) Dhindsa, N.; Chia, A.; Boulanger, J.; Khodadad, I.; LaPierre, R.; Saini, S. S. *Nanotechnology* **2014**, *25* (30), 305303.

(15) Mårtensson, T.; Svensson, C. P. T.; Wacaser, B. A.; Larsson, M. W.; Seifert, W.; Deppert, K.; Gustafsson, A.; Wallenberg, L. R.; Samuelson, L. *Nano Lett.* **2004**, *4* (10), 1987−1990.

(16) Spurgeon, J. M.; Plass, K. E.; Kayes, B. M.; Brunschwig, B. S.; Atwater, H. A.; Lewis, N. S. *Appl. Phys. Lett.* **2008**, *93* (3), 032112.

(17) Heurlin, M.; Magnusson, M. H.; Lindgren, D.; Ek, M.; Wallenberg, L. R.; Deppert, K.; Samuelson, L. *Nature* **2012**, *492* (7427), 90−94.

(18) Metaferia, W.; Persson, A. R.; Mergenthaler, K.; Yang, F.; Zhang, W.; Yartsev, A.; Wallenberg, R.; Pistol, M.-E.; Deppert, K.; Samuelson, L.; Magnusson, M. H. *Nano Lett.* **2016**, *16* (9), 5701−5707.

(19) Björk, M. T.; Ohlsson, B. J.; Sass, T.; Persson, A. I.; Thelander, C.; Magnusson, M. H.; Deppert, K.; Wallenberg, L. R.; Samuelson, L. *Nano Lett.* **2002**, *2* (2), 87−89.

(20) Gudiksen, M. S.; Lauhon, L. J.; Wang, J.; Smith, D. C.; Lieber, C. M. *Nature* **2002**, *415* (6872), 617−620.

(21) Wu, Y.; Fan, R.; Yang, P. *Nano Lett.* **2002**, *2* (2), 83−86.

(22) Glas, F. *Phys. Rev. B: Condens. Matter Mater. Phys.* **2006**, *74* (12), 121302.

(23) Chen, Y.; Pistol, M.-E.; Anttu, N. *Sci. Rep.* **2016**, *6* (1), 32349.

(24) Chen, Y.; Höhn, O.; Tucher, N.; Pistol, M.-E.; Anttu, N. *Opt. Express* **2017**, *25* (16), A665.

(25) Colombo, C.; Heiss, M.; Grätzel, M.; Fontcuberta i Morral, A. *Appl. Phys. Lett.* **2009**, *94* (17), 173108.

(26) Heurlin, M.; Wickert, P.; Fält, S.; Borgström, M. T.; Deppert, K.; Samuelson, L.; Magnusson, M. H. *Nano Lett.* **2011**, *11* (5), 2028−2031.

(27) Holm, J. V.; Jørgensen, H. I.; Krogstrup, P.; Nygård, J.; Liu, H.; Aagesen, M. *Nat. Commun.* **2013**, *4*, 1498.

(28) Mann, S. A.; Oener, S. Z.; Cavalli, A.; Haverkort, J. E. M.; Bakkers, E. P. A. M.; Garnett, E. C. *Nat. Nanotechnol.* **2016**.

(29) Talin, A. A.; Léonard, F.; Katzenmeyer, A. M.; Swartzentruber, B. S.; Picraux, S. T.; Toimil-Molares, M. E.; Cederberg, J. G.; Wang,

DOI: 10.1021/acs.nanolett.8b00494
Nano Lett. 2018, 18, 3038−3046

X.; Hersee, S. D.; Rishinaramangalum, A. *Semicond. Sci. Technol.* **2010**, *25* (2), 024015.
(30) Zhao, S.; Salehzadeh, O.; Alagha, S.; Kavanagh, K. L.; Watkins, S. P.; Mi, Z. *Appl. Phys. Lett.* **2013**, *102* (7), 073102.
(31) Darbandi, A.; Watkins, S. P. *J. Appl. Phys.* **2016**, *120* (1), 014301.
(32) Zeng, X.; Otnes, G.; Heurlin, M.; Mourão, R. T.; Borgström, M. T. *Nano Res.* **2017**, *1*, 1−9.
(33) Salehzadeh, O.; Zhang, X.; Gates, B. D.; Kavanagh, K. L.; Watkins, S. P. *J. Appl. Phys.* **2012**, *112* (9), 094323.
(34) Darbandi, A.; Kavanagh, K. L.; Watkins, S. P. *Nano Lett.* **2015**, *15* (8), 5408−5413.
(35) Otnes, G.; Heurlin, M.; Zeng, X.; Borgström, M. T. *Nano Lett.* **2017**, *17* (2), 702−707.
(36) Mikulik, D.; Ricci, M.; Tutuncuoglu, G.; Matteini, F.; Vukajlovic, J.; Vulic, N.; Alarcon-Llado, E.; Fontcuberta i Morral, A. *Nano Energy* **2017**, *41*, 566−572.
(37) Heurlin, M.; Anttu, N.; Camus, C.; Samuelson, L.; Borgström, M. T. *Nano Lett.* **2015**, *15* (5), 3597−3602.
(38) Chen, Y.; Kivisaari, P.; Pistol, M.-E.; Anttu, N. *Nanotechnology* **2016**, *27* (43), 435404.
(39) Hirt, G.; Hofmann, D.; Mosel, F.; Schäfer, N.; Müller, G. *J. Electron. Mater.* **1991**, *20* (12), 1065−1068.
(40) Liang, B. W.; Lee, P. Z.; Shih, D. W.; Tu, C. W. *Appl. Phys. Lett.* **1992**, *60* (17), 2104−2106.
(41) Dreszer, P.; Chen, W. M.; Seendripu, K.; Wolk, J. A.; Walukiewicz, W.; Liang, B. W.; Tu, C. W.; Weber, E. R. *Phys. Rev. B: Condens. Matter Mater. Phys.* **1993**, *47* (7), 4111−4114.
(42) Temkin, H.; Dutt, B. V.; Bonner, W. A. *Appl. Phys. Lett.* **1981**, *38* (6), 431−433.
(43) Green, M. A. In *Solar Cells*; The University of New South Wales, 1982; pp 85−102.
(44) Kuech, T. F.; Wang, P.-J.; Tischler, M. A.; Potemski, R.; Scilla, G. J.; Cardone, F. *J. Cryst. Growth* **1988**, *93* (1−4), 624−630.
(45) LaPierre, R. R. *J. Appl. Phys.* **2011**, *109* (3), 034311.
(46) Yu, S.; Roemer, F.; Witzigmann, B. *J. Photonics Energy* **2012**, *2*, 028002-1.
(47) Huang, N.; Lin, C.; Povinelli, M. L. *J. Appl. Phys.* **2012**, *112* (6), 064321.
(48) Stringfellow, G. B. *J. Vac. Sci. Technol.* **1976**, *13* (4), 908.
(49) Henry, C. H.; Logan, R. A.; Merritt, F. R. *J. Appl. Phys.* **1978**, *49* (6), 3530−3542.
(50) Reinhardt, K. C.; Yeo, Y. K.; Hengehold, R. L. *J. Appl. Phys.* **1995**, *77* (11), 5763−5772.
(51) Tiwari, S.; Frank, D. J.; Wright, S. L. *J. Appl. Phys.* **1988**, *64* (10), 5009−5012.
(52) Dodd, P. E.; Stellwag, T. B.; Melloch, M. R.; Lundstrom, M. S. *IEEE Trans. Electron Devices* **1991**, *38* (6), 1253−1261.
(53) Espinet-Gonzalez, P.; Rey-Stolle, I.; Ochoa, M.; Algora, C.; Garcia, I.; Barrigon, E. *Prog. Photovoltaics* **2015**, *23* (1), 874−882.
(54) Black, L. E.; Cavalli, A.; Verheijen, M. A.; Haverkort, J. E. M.; Bakkers, E. P. A. M.; Kessels, W. M. M. *Nano Lett.* **2017**, *17* (10), 6287−6294.
(55) Robinson, S. J.; Aberle, A. G.; Green, M. A. *J. Appl. Phys.* **1994**, *76* (12), 7920−7930.
(56) Pudov, A. O.; Sites, J. R.; Contreras, M. A.; Nakada, T.; Schock, H. W. *Thin Solid Films* **2005**, *480−481*, 273−278.
(57) Niemegeers, A.; Burgelman, M. *J. Appl. Phys.* **1997**, *81* (6), 2881−2886.
(58) Chen, Y.; Kivisaari, P.; Pistol, M.; Anttu, N. *Nanotechnology* **2018**, *29* (4), 045401.
(59) Huang, M. L.; Chang, Y. C.; Chang, C. H.; Lee, Y. J.; Chang, P.; Kwo, J.; Wu, T. B.; Hong, M. *Appl. Phys. Lett.* **2005**, *87* (25), 252104.
(60) Hinkle, C. L.; Sonnet, A. M.; Vogel, E. M.; McDonnell, S.; Hughes, G. J.; Milojevic, M.; Lee, B.; Aguirre-Tostado, F. S.; Choi, K. J.; Kim, H. C.; Kim, J.; Wallace, R. M. *Appl. Phys. Lett.* **2008**, *92* (7), 071901.
(61) Yen, C. F.; Yeh, M. Y.; Chong, K. K.; Hsu, C. F.; Lee, M. K. *Appl. Phys. A: Mater. Sci. Process.* **2016**, *122* (7), 1−9.
(62) Mallorquí, A. D.; Alarcón-Lladó, E.; Mundet, I. C.; Kiani, A.; Demaurex, B.; De Wolf, S.; Menzel, A.; Zacharias, M.; Fontcuberta i Morral, A. *Nano Res.* **2015**, *8* (2), 673−681.
(63) Borgström, M. T.; Wallentin, J.; Trägårdh, J.; Ramvall, P.; Ek, M.; Wallenberg, L. R.; Samuelson, L.; Deppert, K. *Nano Res.* **2010**, *3* (4), 264−270.
(64) Leamy, H. J. *J. Appl. Phys.* **1982**, *53* (6), R51−R80.
(65) Hausmann, D.; Becker, J.; Wang, S.; Gordon, R. G. *Science* **2002**, *298* (5592), 402−406.

DOI: 10.1021/acs.nanolett.8b00494
Nano Lett. 2018, 18, 3038−3046